# Structural and Electronic Properties of Micellar Au Nanoparticles: Size and Ligand Effects

Farzad Behafarid,[†] Jeronimo Matos,[†] Sampyo Hong,[†] Lihua Zhang,[‡] Talat Shahnaz Rahman,[†] and Beatriz Roldan Cuenya[§,*]

[†]Department of Physics, University of Central Florida, Orlando, Florida 32816, United States, [‡]Center for Functional Nanomaterials, Brookhaven National Laboratory, Upton, New York 11973, United States, and [§]Department of Physics, Ruhr University Bochum, Bochum, 44780, Germany

ABSTRACT Gaining experimental insight into the intrinsic properties of nanoparticles (NPs) represents a scientific challenge due to the difficulty of deconvoluting these properties from various environmental effects such as the presence of adsorbates or a support. A synergistic combination of experimental and theoretical tools, including X-ray absorption fine-structure spectroscopy, scanning transmission electron microscopy, atomic force microscopy, and density functional theory was used in this study to investigate the structure and electronic properties of small ($\sim$1–4 nm) Au NPs synthesized by an inverse micelle encapsulation method. Metallic Au NPs encapsulated by polystyrene 2-vinylpiridine (PS-P2VP) were studied in the solution phase (dispersed in toluene) as well as after deposition on γ-Al$_2$O$_3$. Our experimental data revealed a size-dependent contraction of the interatomic distances of the ligand-protected NPs with decreasing NP size. These findings are in good agreement with the results from DFT calculations of unsupported Au NPs surrounded by P2VP, as well as those obtained for pure (ligand-free) Au clusters of analogous sizes. A comparison of the experimental and theoretical results supports the conclusion that the P2VP ligands employed to stabilize the gold NPs do not lead to strong distortions in the average interatomic spacing. The changes in the electronic structure of the Au-P2VP NPs were found to originate mainly from finite size effects and not from charge transfer between the NPs and their environment (*e.g.*, Au—ligand interactions). In addition, the isolated ligand-protected experimental NPs only display a weak interaction with the support, making them an ideal model system for the investigation of size-dependent physical and chemical properties of structurally well-defined nanomaterials.
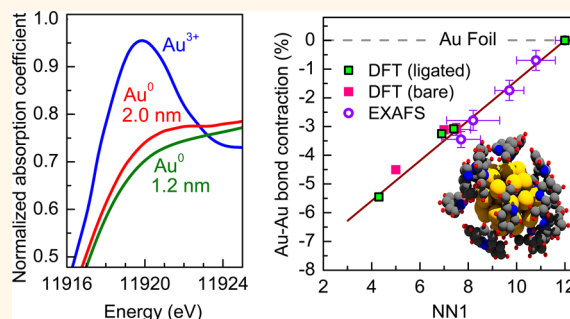
KEYWORDS: Au nanoparticle · strain · size effects · XAFS · EXAFS · XANES · TEM · AFM · DFT · FEFF simulation

The growing interest in the understanding of the physical and chemical properties of Au nanoparticles (NPs) and their evolution with size and environment (*i.e.*, support, ligands, and adsorbates) stems in part from the quest for new commercially viable technologies. In recent years, numerous applications of Au NPs in industrially and societally relevant fields have been demonstrated, including their use as efficient and environmentally friendly catalysts,[1–5] sensor components,[6,7] active and tunable elements in electronic[8] and optical devices, as well as in medicine.[9–13] For example, because of their biocompatibility,[9,14,15] new diagnostic and therapeutic tools such as surface plasmon resonance imaging, two-photon luminescence imaging, and plasmonic photothermal therapy have been developed using Au NPs and applied to the detection[10,11] and destruction of cancer cells.[10,12,13]

The flexibility in the application of Au NPs makes fundamental research of their intriguing properties of crucial importance to their use. Insight on how their optical and chemical response is affected by their electronic properties,[16] geometry (size and shape),[17,18] internal crystalline order, and intrinsic and extrinsic (environment-driven) strain[19,20] is key to engineering new functional nanomaterials. One piece of this puzzle is the size-dependent contraction observed for small NPs with decreasing NP size.[21–27] It is well-known that for small free (unsupported) NPs, surface tension (intrinsic effect) leads to a decrease in the average nearest-neighbor bond length. However, factors like NP/support interactions,[28,29] adsorbates,[30] or
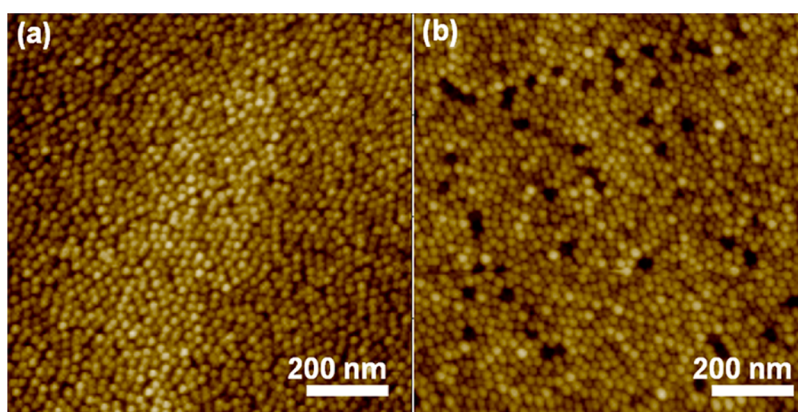
© 2014 American Chemical Society

Figure 1. (a) Tapping-mode AFM images of micelle-synthesized Au NP samples supported on $SiO_2/Si(111)$: (a) S1 and (b) S2.

capping molecules can also result in structural changes in the NPs. For example, Giovanetti *et al.* reported changes in the shape of P2VP-capped Pt NPs upon adsorption on mesoporous silica.[26] Comparatively, for thiol-capped Au and Pd NPs,[24,31,32] interaction with a chemisorbed capping agent was found to induce an expansion in the bond lengths that counteracts the expected size-dependent contraction. Adding even more complexity, varying degrees of contraction have been observed on different surface facets of nanocrystals.[27] Accordingly, the ability to separate these different contributions presents a great experimental challenge, since NPs with modified geometries (size and shape) will be exposed to different degrees of intrinsic as well as extrinsic strain due to the presence of distinct crystalline facets, different NP/support contact areas, and distinct shape-stabilizing surface ligands.

To decouple different environmental effects from the intrinsic size-dependent structural and electronic properties of Au NPs, we have synthesized size-selected Au NPs by a colloidal approach and have isolated them from the support *via* their encapsulation on diblock copolymers. In addition, measurements were conducted on isolated (separated by the ligands), unsupported (in solution), as well as supported (impregnated on nanoscrystalline γ-Al_2O_3) NPs prepared by the same NP solution.

The synergetic combination of X-ray absorption fine-structure spectroscopy (XAFS) experiments and density functional theory (DFT) calculations constitutes a powerful approach to investigate ligand effects on NPs.[33] In this study, XAFS measurements were carried out in order to extract information on the geometry of the NPs, internal degree of structural disorder, strain, and charge transfer and redistribution phenomena. Additional complementary analysis techniques employed to gain insight into the morphology and chemical state of the NPs include high-angle annular dark field scanning transmission electron microscopy (HAADF-STEM), atomic force microscopy (AFM), and X-ray photoelectron spectroscopy (XPS). Moreover, DFT calculations were carried out on clean and

ligand-protected model Au NPs in order to separate size-dependent intrinsic from extrinsic structural effects. FEFF simulations were conducted using the NP structures obtained from DFT, and the theoretical and experimental XANES data were compared in order to explain the origin of the changes observed in the XANES spectra with decreasing NP size.

RESULTS

Morphology, Structure, and Electronic Properties (AFM, STEM, XAS). Figure 1 displays AFM images of micelle-synthesized metallic Au NPs surrounded by the polymeric ligands corresponding to the NP solutions used for the preparation of samples S1 and S2 dip-coated on $SiO_2/Si(111)$. Narrowly size distributed NPs are evidenced.

Smaller NPs are observed *via* HAADF-STEM as compared to AFM, since the former technique does not display the polymeric shell surrounding the metallic Au NP core. Figure 2 shows representative TEM images of samples S2 and S5 together with the corresponding diameter histograms. The remaining NP size histograms are depicted in Supporting Information, Figure S2, and the average values are reported in Table 1.

XANES spectra displaying the normalized Au-L_3 absorption coefficient of ligand-protected metallic Au NPs on γ-Al_2O_3 (samples S1—S5) are shown in Figure 3 together with data from a bulk-like sample (Au foil). For reference, the inset in Figure 3 shows the XANES spectrum of one of our reduced Au NPs (S1) compared to that of a similarly prepared sample containing Au^{3+} NPs (not reduced in solution), both supported on γ-Al_2O_3. For samples S3—S5 (small NPs, $\sim$1 nm), the XANES spectra appear superimposed due to their similarity.

Au-L_3 edge k^2-weighted EXAFS data in k-space of samples S1—S5, are shown in Supporting Information, Figure 4, together with a reference Au foil. Figure S4 displays the magnitude of the Fourier transform of the EXAFS spectra (k^2-weighted) of a gold foil and several Au NP samples (S1, S2, S3, and S5). The strong decrease in the overall amplitude of the EXAFS features of the NPs as compared to bulk Au is assigned to the
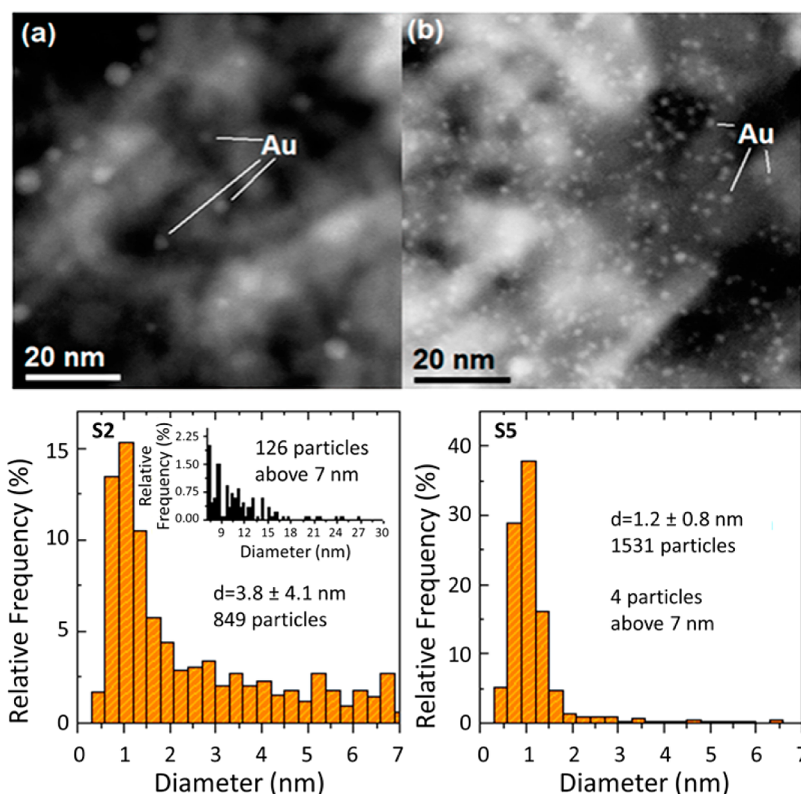
Figure 2. HAADF-TEM (a,b) and bright field TEM (c,d) images of Au NPs on γ-Al$_2$O$_3$ in samples (a,c) S2 and (b,d) S5. The corresponding NP histograms are also provided.

TABLE 1. Summary of Parameters Used for the Synthesis of Metallic Au NPs[a]

sample	polymer	L	average TEM diameter (nm)	EXAFS diameter (nm)
S1	PS(27700)-P2VP(4300)	0.6	2.0 ± 4.7	8.7(N/A)
S2	PS(16000)-P2VP(3500)	0.4	3.8 ± 4.1	1.9 ± 0.5
S3	PS(33000)-P2VP(46000)	0.2	1.1 ± 0.4	1.3 ± 0.5
S4	PS(91000)-P2VP(10000)	0.1	1.2 ± 0.5	1.2 ± 0.2
S5	PS(16000)-P2VP(3500)	0.05	1.2 ± 0.8	1.1 ± 0.2

[a] Includes the molecular weights of the different encapsulating ligands and the metal salt to P2VP ratio (L). The Au loading on the γ-Al$_2$O$_3$ supports was 1%. Also given are the AFM NP heights (including the ligand) and TEM diameters.

decreased NP size and/or increased atomic disorder. The EXAFS data of samples S3−S5 are similar, and therefore, only S3 is plotted here. Furthermore, features corresponding to good long-range atomic ordering (which appear in the 3.5−6 Å range) are only observed for samples containing large NPs (∼2−4 nm, S1 and S2). This could be due to the size effect or the higher disorder expected for small NPs, since they have a lower number of neighbors in higher shells. In addition to the typical Au−Au spectral features, samples S3−S5 also possess a shoulder at low-R (∼1.6 Å phase uncorrected data in Figure 4a and inset) corresponding to a different chemical species (Au-X) assigned to the surrounding ligands. Therefore, the EXAFS data from these samples were fit with a second component to

account for this additional feature, as indicated in the inset of Figure 4a. The Au-X component will be discussed in more detail in view of our DFT calculations.

Although EXAFS data of the unsupported (liquid solutions) NPs were also measured, poor quality data were obtained from the majority of the liquid samples due to their strong dilution in toluene and the thickness of the glass pipet used as container. From the series of samples investigated, the best examples are the unsupported equivalents of samples S2 and S3. The r-space EXAFS spectra of Al$_2$O$_3$-supported and unsupported (liquid) Au NPs from S2 and S3 are shown in Figures 4b and 4c, respectively.

The results of the analysis of the EXAFS spectra displayed in Figure 4 and remaining Au NP samples are shown in Table 2. The Au−Au first NN CNs (NN1) obtained by fitting the spectra agree with the qualitative analysis above and with the sizes extracted from the TEM analysis. EXAFS data in r-space from all samples as well as the theoretical fits are shown in Supporting Information, Figure S5. The fitting parameters are also provided in Supporting Information, Table S1. Sample S1 has an Au−Au NN1 close to the bulk value of 12. The NN1 value of samples S2−S5 ranges from 9.4 ± 0.6 to 6.3 ± 0.8. Assuming 3D fcc NP shapes, the Au−Au NN1 obtained from EXAFS can be used to extract information on the average NP size, as discussed in ref 34. It is important to note that EXAFS is an ensemble-averaging technique. Each atom in a NP
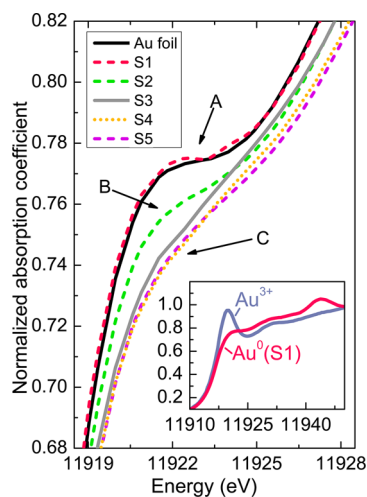
Figure 3. Comparison of the XANES Au-L$_3$ edge white-line intensities for the different reduced Au NP samples synthesized *via* inverse micelle encapsulation and supported on γ-Al$_2$O$_3$ (see Table 1 for details): (A) S1 and a gold reference foil, (B) S2, and (C) S3−S5. The inset shows XANES spectra of reduced gold (S1) and Au^{3+} NPs (chlorine from the Au precursor salt present, HAuCl$_4$). The sample containing Au^{3+} species corresponds to a similar NP solution as S1 but was measured before reduction with NaBH$_4$. All data were measured in air at room temperature.

Figure 4. Au-L$_3$ edge k^2-weighted EXAFS data in *r*-space (Fourier transform *k*-range 2.5−11 Å^{-1}) from reduced Au NPs synthesized *via* inverse micelle encapsulation in PS-P2VP diblock copolymers and supported on γ-Al$_2$O$_3$. (a) Spectra corresponding to samples with different average NP sizes are shown (S1, S2, S3) together with a reference Au foil. The inset in panel a shows a representative fit of the spectrum of sample S5, along with the separate Au−X (likely Au−N) and Au−Au components. Comparison of data obtained from micelle encapsulated NPs before (in liquid solution) and after impregnation on γ-Al$_2$O$_3$: (b) S2 and (c) S3. The inset in panel c is a schematic of how the shape of encapsulated Au NPs might change upon deposition on a support. All data were measured in air at room temperature.

contributes equally to the data, therefore, large NPs carry greater weight in the data. A correlation between the NP size and their internal atomic disorder (σ^2) was also observed *via* EXAFS, with smaller NPs showing higher disorder. In particular, all NPs had a greater disorder than bulk gold (0.0082 Å^2). The highest disorder was found for the smallest NPs S3−S5, (ranging between 0.012 Å^2 and 0.015 Å^2) which was followed by the large NPs in samples S1 and S2 (0.0095 and 0.0119 Å^2, respectively).

Size- and Ligand-Dependent Structure and Electronic Properties: (DFT, XANES Simulations). DFT calculations were performed to better understand the effect of the P2VP ligands on the structure and electronic properties of unsupported Au NPs. Figure 5 shows 3D visualizations of the Au NPs used in the theoretical calculations, with and without ligands, after structural relaxation. Pair distribution functions of all the structures shown in Figure 5 are provided in Figure 6. Smaller Au NPs were found to interact more strongly with the P2VP ligands. As a result, after structural relaxation the shape of the ligated NPs appears more disordered. This is particularly true for Au$_{13}$.

The average numbers of first nearest neighbors (NN1) for all samples are shown in Table 3. NN1 decreases from 5.0 (in the bare NP) to 4.3 (in the ligated NP) for Au$_{13}$, whereas the decrease is rather mild for Au$_{33}$ and Au$_{55}$, that is, from 7.0 to 6.9, and from 7.5 to 7.4, respectively. The average Au−Au distance decreases from 2.822 Å (in bare Au NP) to 2.794 Å (in ligated Au NP) for Au$_{13}$, from 2.863 Å to 2.859 Å for Au$_{33}$, and it does not change for Au$_{55}$ (2.864 Å). It should be considered that large Au NPs have lower surface to bulk ratio and therefore are
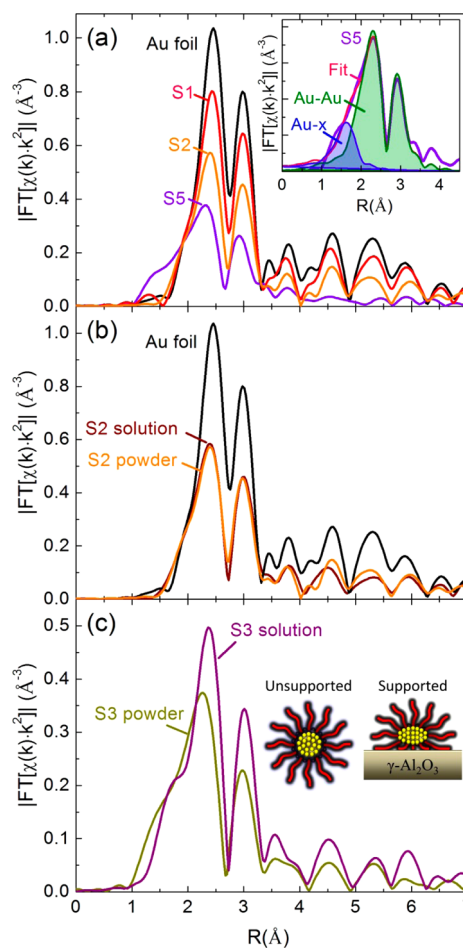
expected to be less affected by the interaction with the P2VP ligands. Large changes in the number of nearest neighbors and bond length suggest strong Au−P2VP interaction and P2VP-induced structural disruption, which were only observed for the smallest theoretical Au NPs (*e.g.*, Au$_{13}$). On the other hand, Au−P2VP interactions appear to be weak in larger NPs such as Au$_{55}$ (~1 nm), which is in the size range of the smallest experimental sample.

In addition to the size-dependent changes in the structural properties of our NPs, modifications of their electronic structure were also observed. Figure 7 shows the calculated *d*-density of states for all structures shown in Figure 5 as well as that of bulk gold. The bare Au$_{13}$ has molecular-like density of states with sharp

TABLE 2. Summary of the Parameters Extracted from the Fit of the Au-L₃ Edge EXAFS Data of Micelle-Synthesized Au NPs Supported on γ-Al$_2$O$_3$[a]

	Au—Au			Au—X		
sample	NN1	R (Å)	σ^2 (Å^2)	NN1	R (Å)	σ^2 (Å^2)
foil	12.0(0.4)	2.870(4)	0.0082(2)			
S1	10.8(0.8)	2.85(1)	0.0095(6)			
S2	9.7(0.6)	2.82(1)	0.0119(6)			
S2-solution	9.8(0.8)	2.83(2)	0.0107 (7)			
S3	8.2 (1.1)	2.79(1)	0.015(2)	0.7(3)	2.11(2)	0.006(6)
S3-solution	9.4(1.2)	2.84(1)	0.012(1)	0.2(3)	2.09(3)	0.004(9)
S4	7.7(0.8)	2.771(8)	0.014(1)	0.7(2)	2.10(1)	0.005(4)
S5	7.5(0.6)	2.781(6)	0.014(1)	0.7(3)	2.11(1)	0.008(5)

[a] These include the 1st nearest neighbor (NN) coordination number (NN1), 1st NN interatomic distance (R), and EXAFS Debye—Waller factor (σ^2). The spectra of the samples containing large NPs (S1, S2) were fitted with only one component corresponding to metallic Au—Au bonds, while those of the small NPs (S3—S5) were fitted with two components, Au—Au metal and Au—X bonds.
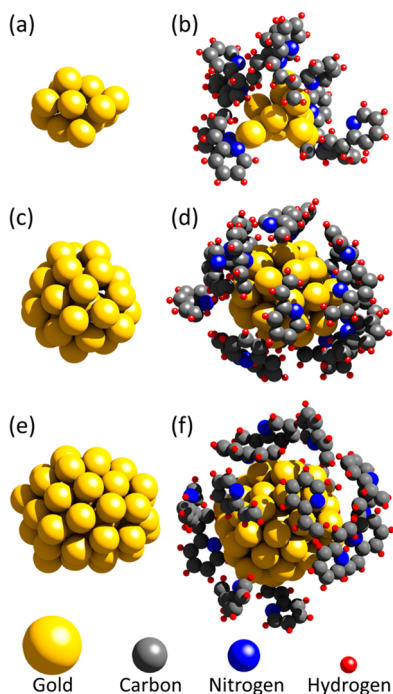

Figure 5. 3D visualization of structurally relaxed (DFT) bare Au NPs: (a) Au$_{13}$, (c) Au$_{33}$, and (e) Au$_{55}$ as well Au NPs ligated with P2VP: (b) Au$_{13}$ (d) Au$_{33}$, and (f) Au$_{55}$.

peaks at certain energies, whereas the larger Au NPs have already continuous solid-like band structure. The attachment of P2VP ligands transforms the density of states of Au$_{13}$ into a continuous band structure, and results in the widening of the bandwidth and left-shifting of the DOS (to lower energy), which could be clearly seen in the density of states of the Au$_{13}$ NP, Figure 7a. Bader charge transfer analysis did not show any significant charge transfer between the ligands and the Au NPs. Therefore, the observed white line suppression in the experimental data should mainly
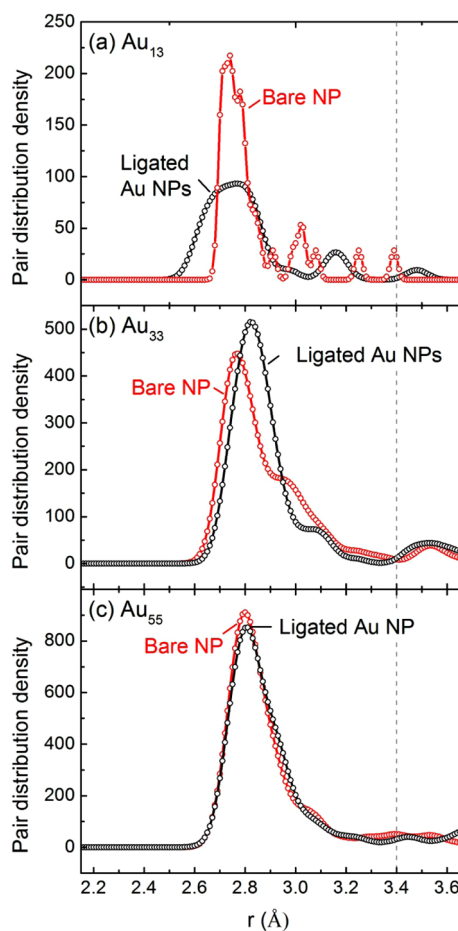

Figure 6. Au—Au pair distribution density for bare and P2VP ligated as Au NPs with (a) 13 atoms, (b) 33 atoms, (c) 55 atoms. The area under the curves represents the number of Au—Au bonds in a certain r-range. The r-cutoff value of 3.4 Å is shown with a vertical dashed line.

have an intrinsic origin due to finite size effects in the NPs.

To better understand the electronic structure of our Au NPs, XANES simulations were carried out using the FEFF 9.6.4 code,[35] Figure 8a. The atomic structures used for the FEFF simulations were those obtained from DFT calculations for Au$_{55}$ and Au$_{55}$ + P2VP NPs including Au, N, C, and H atoms (259 atoms in total). Since with the present software XANES simulations could only be carried out for one absorbing atom at a time, a separate code was written to generate FEFF input files with different Au absorbing atoms (55 input files) and also to collect and combine the data of all atoms after running the FEFF code. Unique potentials were assigned to the first 24 nearest neighbors (covering all the first and second shell neighbors) of the adsorbing atoms, while the potentials for atoms further away were considered to be the same. The final XANES spectrum was obtained by averaging all the XANES data calculated for individual atoms. Figure 8a shows the simulated XANES data for bulk Au, Au$_{55}$, and Au$_{55}$+P2VP (main panel) as well as the experimental

TABLE 3. Summary of Average Bond Lengths for Calculated Au—Au, Au—N, and Au—C from DFT Calculations for Au$_{13}$, Au$_{33}$, and Au$_{55}$ Encapsulated with P2VP Polymer^a

	d_{Au-Au} (rc = 3.400 Å)	d_{Au-N} (rc = 2.587 Å)	d_{Au-C} (rc = 2.650 Å)	NN1 Au—Au	no. of Au—N	no. of Au—C
Au$_{13}$	2.822			5.0		
Au$_{33}$	2.863			7.0		
Au$_{55}$	2.864			7.5		
Au$_{13}$ (P2VP)$_{10}$	2.794	2.25	2.10	4.3	7	2
Au$_{33}$ (P2VP)$_{16}$	2.859	2.48	2.44	6.9	4	6
Au$_{55}$ (P2VP)$_{16}$	2.864	2.30	2.28	7.4	4	6

^{a} NN1 coordination numbers are provided for Au—Au bonds as well as for Au—N and Au—C bonds. Note that rc (*r*-cutoff) is 3.40 Å, 2.59 Å, and 2.65 Å (or 1.25 × *r*-covalent, which is 2.72 Å, 2.07 Å, and 2.12 Å for Au—Au, Au—N, and Au—C bonds, respectively). The Au—Au bond length obtained for bulk gold is 2.955 Å.
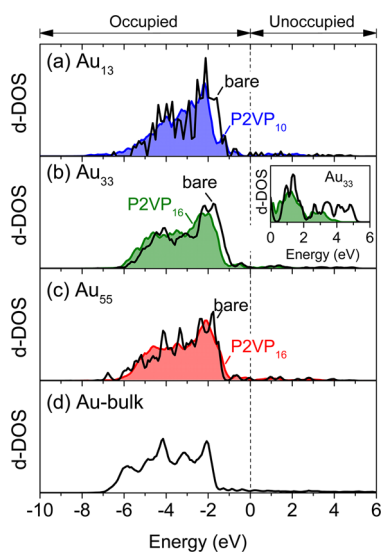

Figure 7. Calculated density of states of bare Au and Au—P2VP structures for (a) Au$_{13}$, (b) Au$_{33}$, (c) Au$_{55}$, and (d) bulk. Shaded curves represent the ligated structures (Au—P2VP), and solid lines represent the bare NPs and bulk structure. The inset in (b) displays the unoccupied portion of the d-DOS of Au$_{33}$.

data obtained from bulk gold and sample S3 (inset). Sample S3 was chosen for comparison since it has a similar size as Au$_{55}$ (~1 nm). It could be seen that the XANES simulation of the Au-L$_3$ edge reproduces a white line shoulder for bulk gold similar to that observed in our experimental data. Additionally, the simulation of the Au$_{55}$ NP reproduces the suppression of the white line observed in the experimental data of the similarly sized NPs in S3.

DISCUSSION

The role of the NP size and NP environment (ligand- and support-effects) on the structure and electronic properties of Au NPs was investigated. From the XANES data shown in Figure 3 it is evident that the intensity of the absorption edge peak (white line) of sample S1 is almost identical to that of the Au foil (labeled A), while a decrease in intensity is observed for sample S2 (labeled B) and S3—S5 (labeled C). The white line in Au-L$_3$ spectra is proportional to the empty 5d electron density of states. This is because the Au-L$_3$ absorption
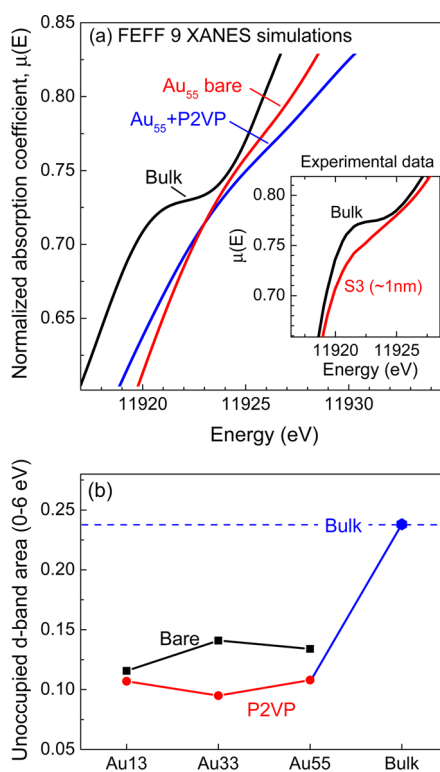

Figure 8. (a) FEFF 9 simulation of the Au-L$_3$ XANES region for bulk gold, Au$_{55}$, and Au$_{55}$+P2VP structures. The atomic coordination of the relaxed model shapes (DFT) shown in Figure 5e and f were used in the input file for FEFF calculations. The inset in panel a shows the experimental XANES data obtained for bulk gold and S3 which has a similar size to Au$_{55}$ (~1 nm). Both experimental data and simulation show that the white line shoulder in the bulk Au data disappears for Au$_{55}$ NPs. (b) Unoccupied d-states area obtained from the data shown in Figure 7(a–d) by integration from 0 to 6 eV above the Fermi level. The decreased unoccupied densities for NPs as compared to bulk structure explains the disappearance of the white line shoulder for the NPs.

edge corresponds to the transition of 2p$_{3/2}$ electrons to empty states in the 5d$_{5/2}$ and 5d$_{3/2}$ levels. Our DFT calculations show that in case of Au, most of *d* band states (>97.5%) are occupied and the portion of the unoccupied *d* levels is minor. Therefore, bulk Au and reduced Au NPs feature a white line that appears only as a shoulder in contrast to a sharp peak observed in the case of some other metals such as Pt.[34,36]

In general, any increase in white line intensity is indicative of an increase in the number of unoccupied *d* states. The latter is observed in our experimental data when cationic gold species are present (unreduced chlorinated Au^{3+} micellar solution), as illustrated in the inset of Figure 3. Other studies have also reported decreased white line intensity for NPs as compared to bulk gold.[37] Changes in the white line intensity might be of extrinsic nature due to the interaction of the Au NPs with their surroundings, including the support, adsorbates, or ligands.

As it was mentioned in the theory section, the Bader charge analysis in our study did not show any significant charge transfer from Au atoms to the ligands or vice versa. Therefore, the decrease in white line peak with decreasing NP size cannot be explained based on ligand−NP charge transfer. Moreover, the FEFF calculations for both free and ligated Au_{55} NPs also reveal the disappearance of the white line shoulder as compared to bulk Au. The latter demonstrate that this finding does not originate from ligand effects and should be due to a finite size effect.

To gain additional insight into the origin of the lower white line intensity of the NPs with respect to bulk gold we would like to refer to the electron density of states calculations (DFT) shown in Figure 7. A correlation exists between the white line intensity and the density of empty states in the d band. Figure 8b displays the area of the unoccupied portion of the d-DOS shown in Figure 7. Interestingly, in the 0−6 eV energy range, the area of the unoccupied d-DOS of all Au NPs (bare and ligated) is almost half of that of bulk Au, suggesting that the reduction of white line intensity in the NPs is intrinsic and originates from NP size effects.[38] Nevertheless, the presence of ligands seems to further decrease the unoccupied DOS as compared to the model bare NPs.

Further knowledge on size-dependent changes in the structure of the NPs was obtained based on EXAFS measurements. Figure 4 shows the *r*-space EXAFS data of supported (Al_2O_3) and unsupported (liquid solution, dispersed in toluene) Au NPs. In both cases, the experimental NPs are separated from each other by PS ligands. The EXAFS data of the large NPs in S2 (supported) and S2s (liquid) are quite similar, Figure 4b, while clear differences are observed for the smaller NPs in S3, Figure 4c. For the small NPs in S3, a decrease in the first nearest neighbor (NN1) coordination number (CN) was detected upon deposition on the support. Since a change in the NP size (a decrease) is not expected upon impregnation on the substrate, we interpret the change in CN as a change in the NP shape from 3D to flat or truncated clusters. Alternatively, an increase in the atomic disorder due to the formation of Au-substrate bonds might also take place. The latter possibility is ruled out due to the presence of the PS ligands surrounding the metallic Au NP core. The

schematic shown in Figure 4c as inset illustrates the observed NP flattening upon deposition on γ-Al_2O_3. A similar observation was previously reported by Giovanetti *et al.*[26] for PVP-capped Pt NPs before and after deposition on mesoporous silica.

In addition to the difference in size between the NPs in S2 and S3, those in S2 lack of the Au-X component found in samples S3−S5, which was assigned to the Au−ligand interaction. The same component might however be also present for the larger NPs in samples S1−S2, but outside our detection limit. Since all Au atoms within a NP contribute equally to the EXAFS signal, for large NPs with a low surface to bulk ratio, the contribution of Au−ligand atomic bonds at the NP surface is expected to be small. From our DFT calculations, the Au species from the $HAuCl_4$ precursor were found to bind to both N and C in the P2VP core of the reverse micelles. According to our calculations, if the Au NPs are large, as in Au_{55} (Figure 5e,f) and Au_{33} (Figure 5c,d), Au−C bonding is dominant, whereas if the NPs are small and the surface more corrugated and disordered, as in case of Au_{13} (Figure 5a,b), Au−N bonding becomes dominant. For example, the number of Au−N bonds versus the number of Au−C bonds is 7:2 for Au_{13}, but 4:6 for Au_{55}. This transition from Au−N to Au−C binding with increasing NP size likely originates from steric limitations that the NC_7H_7 rings face when making bonds with Au atoms *via* the N atoms. Due to these limitations, Au−N bond formation is easier on a rough surface where some Au atoms slightly protrude from the surface (*e.g.*, Au_{13}) as compared to the surface of larger NPs with lower curvature (*e.g.*, Au_{55}). The calculated Au−X (X=N and C) bond lengths (see Table 3) are in reasonable agreement (although slightly larger) with the Au−X distance of $\sim$2.1 Å obtained experimentally, suggesting that such a component observed in the fits of the EXAFS data of our small Au NPs at low *r* values could correspond to both Au−C and Au−N bonds with a more prominent contribution from Au−C bonds. It should be noted that a larger distance was also obtained by DFT for bulk Au (2.96 Å) as compared to the experimental value extracted by EXAFS (2.87 Å), which might explain the somewhat larger calculated Au−C and Au−N distances.

To separate intrinsic (size/shape) from extrinsic effects (ligand, adsorbate, support) on the structural and electronic properties of small NPs, we have summarized the results from our EXAFS analysis of size-controlled PS-P2VP-encapsulated Au NPs and compared with related data from the literature. Figure 9a shows Au−Au distances extracted *via* EXAFS as a function of NN1. A clear decrease of the Au−Au distances is observed with decreasing coordination number, with our data from the micellar NPs having the largest contractions among all experimental systems shown. Among the previous experimental reports, that of Marcus *et al.*[39] reported a comparable Au−Au bond contraction for
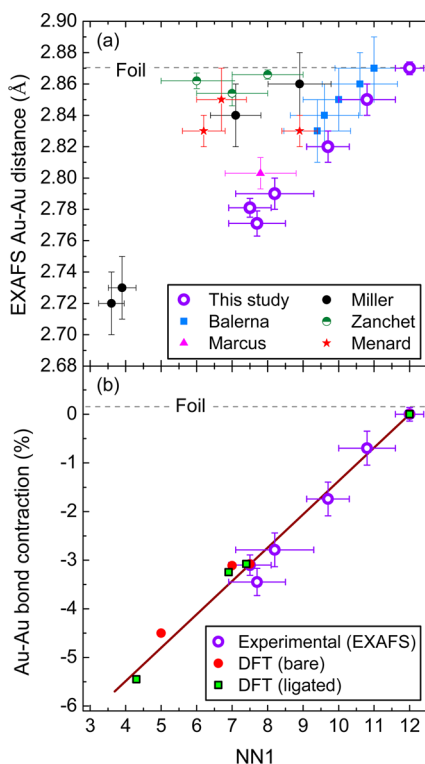
Figure 9. (a) Au—Au distance vs first nearest neighbor coordination number obtained from the fitting of EXAFS spectra for PS-P2VP-encapsulated metallic Au NPs supported on γ-Al_2O_3: S1—S5, along with a reference Au foil. Also plotted for comparison are Au—Au distances extracted from the literature for Au NPs synthesized *via* several different methods.[23,24,37,39,40] (b) Plot of the Au—Au bond contraction *vs* first nearest neighbor coordination number comparing our theoretical (DFT) results for ligand-free and P2VP-encapsulated Au_{13}, Au_{33}, and Au_{55} NPs to our experimental results for samples S1—S5 (EXAFS). The Au—Au bond contraction was defined as $100 \times (L_{NP} - L_{Bulk})/L_{Bulk}$. The theoretical contractions were obtained using the DFT calculated bond length of 2.955 Å for bulk Au—Au (L_{Bulk}) as reference, while the experimental contractions were calculated using a bond length of 2.870 Å obtained from EXAFS analysis of the data from a Au foil. The line in panel b is a guide for the eye.

Au_{55} clusters protected by triphylphosphine ligands.[39] Balerna *et al.*[23] also reported similar contractions for physical-vapor-deposited Au NP/Mylar film multilayers.[23] Au NPs ligated with sulfur-containing molecules displayed the largest Au—Au distances and lowest contractions, illustrating the key role of the protecting ligands in the structural and consequently electronic properties of small NPs.[24,40] A similar decrease has been previously reported by Miller *et al.*[37] on small Au NPs prepared by the deposition/impregnation method on silica, alumina, titania, niobia, and zirconia and was assigned to intrinsic size effects.[37]

The fact that the largest bond contraction was observed in our study could be assigned to specifics of our weak Au—ligand interaction or to the fact that our samples contain size-controlled NPs, with likely a smaller fraction of larger NPs as those available in previous literature reports, which results in more clear size-dependent trends. Also as it has been previously

shown, the interaction could partially lift the bond contraction induced by the finite size effect.[24,33,41] However, our DFT calculations on small NPs do not show such a decrease in the bond length contraction for the P2VP-ligated as compared to bare NPs. From our theoretical calculations, the P2VP—Au interaction is weak and has no effect on the bond length for NPs larger than 1 nm, which includes all NP sizes in our experiments. Therefore, the larger contraction observed in our study could be understood in terms of our ligated NPs behaving similarly to completely bare NPs and therefore, they show the maximum contraction expected from finite size effects. Other studies have also shown that the P2VP interaction with Au NPs is weak to a degree that would allow the NP surface to be still available for catalytic reactions.[42]

Finally, we would like to note that the comparison of the size-dependent experimental and theoretical contractions of the first nearest neighbor interatomic distances shown in Figure 9b reveals that the bond length contraction obtained by DFT follows the same linear trend observed in our experimental data, and thus in fact is in accord with experiment. The larger bond contraction obtained for both bare and ligated Au NPs as compared to bulk Au indicates stronger Au—Au interaction in NPs. Since the Au—Au interaction is dominated by d—d and s—d hybridization, a stronger interaction means more electron density in the 5d and 6s orbitals (less electron density in 6p),[38] which explains the lower unoccupied d-DOS density observed in our study for all NPs as compared to bulk gold.

In summary, it was shown that a combination of different experimental and theoretical techniques such as HAADF-STEM, XANES, EXAFS, DFT, and FEFF simulation is crucial in order to shed light into the morphology, electronic structure, charge transfer, and redistribution phenomena in complex nanoscale systems such as the one at hand.

CONCLUSIONS

Gold NPs with different average sizes were synthesized by encapsulation in PS-P2VP reverse micelles, and the interaction of the Au atoms with the P2VP ligands was studied experimentally (HAADF-STEM, EXAFS/XANES) and theoretically (DFT and FEFF simulations). Through a synergistic comparison with DFT data from pure and P2VP-ligated Au NPs, intrinsic and extrinsic factors affecting the structural and electronic properties of the NPs could be distinguished.

We have used XAFS and STEM to probe interactions between Au NPs and PS-P2VP polymeric ligands as a function of the Au particle size. A contraction of the interatomic distances with decreasing NP size was observed. Such change was found to be larger than those previously reported for other related systems. The comparison of theoretical (DFT) and experimental (EXAFS) data from pure and P2VP-protected Au NPs

revealed a relatively low interaction of the Au atoms with the P2VP ligands for NPs larger than ∼1 nm.

Experimentally, a decrease in the XANES white line intensity of our micellar metallic Au NPs as compared to bulk gold was observed with decreasing NP size. Such a decrease, together with an overall diminution in the area of the Au-L$_3$ absorption edge is indicative of a reduction in the unoccupied d-state electron density. On the basis of DFT calculations it was shown that this reduction is intrinsic in nature, and is due to NP finite size effects rather than to Au−ligand interactions or charge transfer.

In summary, the present work illustrates the achievement of a model experimental nanoparticle system created *via* colloidal chemistry with electronic and structural properties only minimally affected by the stabilizing PS-P2VP ligands. The latter characteristic makes it an ideal target for experimental research on small, size-controlled nanoparticles which can be directly compared with bare theoretical clusters.

METHODS

Sample Preparation. NP synthesis was started by dissolving polystyrene 2-vinylpiridine (PS-P2VP) diblock copolymers with different molecular weights in toluene in order to create inverse micelles. Subsequently, the micellar cages were loaded with HAuCl$_4$. The NP size was tuned by either changing the length of the polymer head (P2VP group), or by changing the metal−salt to P2VP ratio for a given encapsulating diblock copolymer. The resulting Au-loaded micelle solutions were then reduced by the addition of NaBH$_4$ with a HAuCl$_4$ to NaBH$_4$ molar ratio of 1:60. NP reduction was evidenced by a change in the color of the solutions from light yellow to red/dark purple. A fraction of each solution was then mixed with nanocrystalline γ-Al$_2$O$_3$ and dried in air at 60 °C while stirring. The rest was kept for NP size analysis *via* AFM and XAFS work in the liquid phase. For comparison, a sample containing nonreduced Au^{3+} NPs was also measured. More details on the sample preparation parameters are given in Table 1.

Sample Characterization. The chemical composition of our Al$_2$O$_3$-supported NPs was investigated *via* XPS (see Supporting Information, Figure S1). A monochromatic X-ray source (Al Kα = 1486.6 eV, SPECS GmbH) operating at 250 W was used. XPS spectra from the Au-4f core level region confirmed the reduction of gold from Au^{3+} to Au^0, and also showed the expected C-1s peak (present in the encapsulating polymer) as well as the absence of a chlorine signal (from the precursor salt) in the sample.

AFM images of the micellar Au NP solutions dip-coated on SiO$_2$/Si(111) wafers were acquired at room temperature in air in tapping mode using a VEECO Nanoscope IIIa microscope (Figure 1). HAADF-STEM was used to characterize the size of the supported Au NPs. The measurements were conducted in an aberration-corrected TEM microscope, JEOL2100F operating at 200 kV. The HAADF-STEM technique was selected for this study due to its high *Z* (atomic number) sensitivity and a probe size of 0.2 nm that produces images with good contrast between small metal NPs and their support. Unfortunately, the dark field imaging mode does not allow the extraction of information about structural characteristics such as interatomic distances or NP shape. In addition, it also does not display the carbonaceous polymeric ligands, and care must be taken when constructing NP size histograms to distinguish individual adjacent NPs. In the analysis of the HAADF-STEM measurements, the diameters of the Au NPs were obtained by measuring the full width at half-maximum. A minimum of 500 particles were measured per sample. STEM measurements were acquired in different regions of each of the samples, and at different magnifications. The average TEM diameter and standard deviation are shown in Table 1, and the histograms are shown in Figure 2 and Supporting Information, Figure S2.

XAFS measurements were performed at beamline X18B of the National Synchrotron Light Source (NSLS) at Brookhaven National Laboratory. The experiments were carried out in transmission mode at the Au-L$_3$ edge (11917 eV). The data were acquired at room temperature in air. A spectrum of a gold foil was recorded as reference in parallel to each NP measurement for alignment purposes. Each NP sample (unsupported) was measured in liquid solution as well as supported on nanocrystalline γ-Al$_2$O$_3$ in the form of thin pellets. The liquid samples were measured inside a pipet with a thin glass wall. For each of the samples, multiple spectra were acquired and averaged to improve the signal-to-noise ratio. Initial processing of the XAFS data was performed using the program Athena,[43] which is based on IFFEFIT.[44] A first shell extended X-ray absorption fine-structure spectroscopy (EXAFS) analysis was conducted in Artemis,[43] (also based on IFFEFIT[44]) using the FEFF8[45] code in order to extract coordination numbers, interatomic distances, and EXAFS Debye−Waller factors. The details of the EXAFS analysis are provided in the supplementary documents.

Theoretical Details. DFT[46,47] calculations were performed to investigate the formation of the reduced Au NPs inside the polymeric micelles within the projector augmented wave method[48] implemented in the Vienna *ab initio* simulation package (VASP).[49,50] The formation of the Au NPs inside the micellar nanoreactors was modeled by creating an encapsulating P2VP layer (polymer head) around the Au precursor units. P2VP ligands (see Supporting Information, Figure 3) were approximated by a set of NC$_7$H$_7$ molecules. Since experimental data for the number of the P2VP units attached to each Au NP are not available, we had to estimate the optimum number of P2VP units needed to describe the experimental Au−P2VP interaction on the basis of the fact that the size of the Au NPs is proportional to the molecular weight of the P2VP component. P2VP units were attached to Au NPs proportionally to the number of Au atoms in each NP. For example, we used 10 NC$_7$H$_7$ units for Au$_{13}$. However, we found that 16 NC$_7$H$_7$ units for Au$_{33}$ were adequate for simulation, since they maximized the ligand coverage possible on the limited surface area of the corresponding Au NP. For Au$_{55}$ we used the same 16 units as for Au$_{33}$ due to computational limitations. However, many of the 16 ligands considered for Au$_{55}$ would not attach to the surface, and therefore, the number of ligands chosen should be enough to describe our experimental system. The resulting Au−P2VP systems have 163, 273, and 295 atoms in total, respectively.

The supercell used in the calculations of the Au−P2VP complexes had dimension of 30 Å × 30 Å × 30 Å. Because of the large size of the supercell used, only a single *k*-point was sufficient for sampling the Brillouin zone. We used a Fermi-level smearing of 0.2 eV. Exchange-correlation energy is included in the calculation using the Perdew−Burke−Enzerhof functional.[51] The cutoff energy for plane-waves was 400 eV. The threshold for electronic energy convergence was set to 1×10^{-4} eV, and that for structural optimization was set to $<1 \times 10^{-2}$ eV/Å. Our calculated bulk lattice constant was 4.18 Å, 2.4% larger than the experimental lattice constant (4.08 Å). The effect of the van der Waals interaction on the geometry of the Au−P2VP complex was checked in our calculations, for example, for the Au$_{55}$−P2VP complex.[52,53] However, no significant difference was observed when the van der Waals interaction was considered. The angular-momentum-decomposed local density of states (DOS) of the NPs was calculated by projecting the wave function into the PAW sphere at each Au atom. The bond length cutoff values (*r*-cutoff) used to determine the first nearest neighbor interaction were defined

as $1.25 \times r$-covalent, which is the sum of two covalent radii (1.36 Å for Au, 0.71 Å for N, 0.76 Å for C)[54] provided the cut off values were 3.40 Å, 2.59 Å, and 2.65 Å for Au−Au, Au−N, and Au−C bonds, respectively. Bader charge analysis was also performed to investigate the charge transfer/redistribution induced by the interaction of the gold NPs with the encapsulating ligands. XANES simulations were done using the FEFF 9.6.4[35] code by introducing the relaxed structures obtained from DFT calculations.

Conflict of Interest: The authors declare no competing financial interest.

Supporting Information Available: Additional XPS data; TEM images and corresponding histograms; raw k-space and theoretically fitted r-space EXAFS data as well as the EXAFS fitting parameters. This material is available free of charge *via* the Internet at http://pubs.acs.org.

REFERENCES AND NOTES

1. Haruta, M. Low-Temperature Oxidation of CO over Gold Supported on TiO$_2$, α-Fe$_2$O$_3$, and Co$_3$O$_4$. *J. Catal.* **1993**, *144*, 175–192.

2. Costello, C. K.; Kung, M. C.; Oh, H. S.; Wang, Y.; Kung, H. H. Nature of the Active Site for CO Oxidation on Highly Active Au/γ-Al$_2$O$_3$. *Appl. Catal. A: Gen* **2002**, *232*, 159–168.

3. Idakiev, V.; Tabakova, T.; Yuan, Z. Y.; Su, B. L. Gold Catalysts Supported on Mesoporous Titania for Low-Temperature Water−Gas Shift Reaction. *Appl. Catal. A: Gen* **2004**, *270*, 135–141.

4. Corti, C. W.; Holliday, R. J.; Thompson, D. T. Progress Towards the Commercial Application of Gold Catalysts. *Top. Catal.* **2007**, *44*, 331–343.

5. Grisel, R. J. H.; Nieuwenhuys, B. E. A Comparative Study of the Oxidation of CO and CH$_4$ over Au/MO$_x$/Al$_2$O$_3$ Catalysts. *Catal. Today* **2001**, *64*, 69–81.

6. Evans, S. D.; Johnson, S. R.; Cheng, Y. L.; Shen, T. Vapour Sensing Using Hybrid Organic−Inorganic Nanostructured Materials. *J. Mater. Chem.* **2000**, *10*, 183–188.

7. Krasteva, N.; Besnard, I.; Guse, B.; Bauer, R. E.; Müllen, K.; Yasuda, A.; Vossmeyer, T. Self-Assembled Gold Nanoparticle/Dendrimer Composite Films for Vapor Sensing Applications. *Nano Lett.* **2002**, *2*, 551–555.

8. Huang, D.; Liao, F.; Molesa, S.; Redinger, D.; Subramanian, V. Plastic-Compatible Low Resistance Printable Gold Nanoparticle Conductors for Flexible Electronics. *J. Electrochem. Soc.* **2003**, *150*, G412–G417.

9. Connor, E. E.; Mwamuka, J.; Gole, A.; Murphy, C. J.; Wyatt, M. D. Gold Nanoparticles Are Taken up by Human Cells and Do Not Cause Acute Cytotoxicity. *Small* **2005**, *1*, 325–327.

10. Huang, X.; El-Sayed, I. H.; Qian, W.; El-Sayed, M. A. Cancer Cell Imaging and Photothermal Therapy in the Near-Infrared Region by Using Gold Nanorods. *J. Am. Chem. Soc.* **2006**, *128*, 2115–2120.

11. Durr, N. J.; Larson, T.; Smith, D. K.; Korgel, B. A.; Sokolov, K.; Ben-Yakar, A. Two-Photon Luminescence Imaging of Cancer Cells Using Molecularly Targeted Gold Nanorods. *Nano Lett.* **2007**, *7*, 941–945.

12. Zharov, V. P.; Galitovskaya, E. N.; Johnson, C.; Kelly, T. Synergistic Enhancement of Selective Nanophotothermolysis with Gold Nanoclusters: Potential for Cancer Therapy. *Laser. Surg. Med.* **2005**, *37*, 219–226.

13. Pitsillides, C. M.; Joe, E. K.; Wei, X.; Anderson, R. R.; Lin, C. P. Selective Cell Targeting with Light-Absorbing Microparticles and Nanoparticles. *Biophys. J.* **2003**, *84*, 4023–4032.

14. Villiers, C. L.; Freitas, H.; Couderc, R.; Villiers, M.-B.; Marche, P. N. Analysis of the Toxicity of Gold Nano Particles on the Immune System: Effect on Dendritic Cell Functions. *J. Nanopart. Res.* **2009**, *12*, 55–60.

15. Shukla, R.; Bansal, V.; Chaudhary, M.; Basu, A.; Bhonde, R. R.; Sastry, M. Biocompatibility of Gold Nanoparticles and Their Endocytotic Fate Inside the Cellular Compartment: A Microscopic Overview. *Langmuir* **2005**, *21*, 10644–10654.

16. Sá, J.; Szlachetko, J.; Kleymenov, E.; Lothschütz, C.; Nachtegaal, M.; Ranocchiari, M.; Safonova, O. V.; Servalli, M.; Smolentsev, G.; van Bokhoven, J. A. Fine Tuning of Gold Electronic Structure by IRMOF Post-Synthetic Modification. *RSC Adv.* **2013**, *3*, 12043–12048.

17. Sánchez-Iglesias, A.; Pastoriza-Santos, I.; Pérez-Juste, J.; Rodríguez-González, B.; García de Abajo, F. J.; Liz-Marzán, L. M. Synthesis and Optical Properties of Gold Nanodecahedra with Size Control. *Adv. Mater.* **2006**, *18*, 2529–2534.

18. Cho, A. Connecting the Dots to Custom Catalysts. *Science* **2003**, *299*, 1684–1685.

19. Xu, Y.; Mavrikakis, M. Adsorption and Dissociation of O$_2$ on Gold Surfaces: Effect of Steps and Strain. *J. Phys. Chem. B* **2003**, *107*, 9298–9307.

20. Mavrikakis, M.; Hammer, B.; Nørskov, J. Effect of Strain on the Reactivity of Metal Surfaces. *Phys. Rev. Lett.* **1998**, *81*, 2819–2822.

21. Huang, Z.; Thomson, P.; Di, S. Lattice Contractions of a Nanoparticle Due to the Surface Tension: A Model of Elasticity. *J. Phys. Chem. Solids* **2007**, *68*, 530–535.

22. Vogel, W.; Bradley, J.; Vollmer, O.; Abraham, I. Transition from Five-Fold Symmetric to Twinned FCC Gold Particles by Thermally Induced Growth. *J. Phys. Chem. B* **1998**, *102*, 10853–10859.

23. Balerna, A.; Bernieri, E.; Picozzi, P.; Reale, A.; Santucci, S.; Burattini, E.; Mobilio, S. Extended X-Ray-Absorption Fine-Structure and Near-Edge-Structure Studies on Evaporated Small Clusters of Au. *Phys. Rev. B* **1985**, *31*, 5058–5065.

24. Zanchet, D.; Tolentino, H.; Martins Alves, M. C.; Alves, O. L.; Ugarte, D. Inter-Atomic Distance Contraction in Thiol-Passivated Gold Nanoparticles. *Chem. Phys. Lett.* **2000**, *323*, 167–172.

25. Pinto, A.; Pennisi, A.; Faraci, G.; D'Agostino, G.; Mobilio, S.; Boscherini, F. Evidence for Truncated Octahedral Structures in Supported Gold Clusters. *Phys. Rev. B* **1995**, *51*, 5315–5321.

26. Giovanetti, L. J.; Ramallo-López, J. M.; Foxe, M.; Jones, L. C.; Koebel, M. M.; Somorjai, G. A.; Craievich, A. F.; Salmeron, M. B.; Requejo, F. G. Shape Changes of Pt Nanoparticles Induced by Deposition on Mesoporous Silica. *Small* **2012**, *8*, 468–473.

27. Huang, W. J.; Sun, R.; Tao, J.; Menard, L. D.; Nuzzo, R. G.; Zuo, J. M. Coordination-Dependent Surface Atomic Contraction in Nanocrystals Revealed by Coherent Diffraction. *Nat. Mater.* **2008**, *7*, 308–313.

28. Giorgio, S.; Henry, C. R.; Pauwels, B.; Van Tendeloo, G. Au Particles Supported on (110) Anatase-TiO$_2$. *Mat. Sci. Eng. A-Struct.* **2001**, *297*, 197–202.

29. Behafarid, F.; Roldan Cuenya, B. Nanoepitaxy Using Micellar Nanoparticles. *Nano Lett.* **2011**, *11*, 5290–5296.

30. Sun, C. Q. Oxidation Electronics: Bond−Band−Barrier Correlation and Its Applications. *Prog. Mater Sci.* **2003**, *48*, 521–685.

31. Crespo, P.; Litrán, R.; Rojas, T.; Multigner, M.; de la Fuente, J.; Sánchez-López, J.; García, M.; Hernando, A.; Penadés, S.; Fernández, A. Permanent Magnetism, Magnetic Anisotropy,

and Hysteresis of Thiol-Capped Gold Nanoparticles. *Phys. Rev. Lett.* **2004**, *93*, 087204.

32. Corthey, G.; Rubert, A. A.; Picone, A. L.; Casillas, G.; Giovanetti, L. J.; Ramallo-López, J. M.; Zelaya, E.; Benitez, G. A.; Requejo, F. G.; José-Yacamán, M.; *et al.* New Insights into the Chemistry of Thiolate-Protected Palladium Nanoparticles. *J. Phys. Chem. C* **2012**, *116*, 9830–9837.

33. Yancey, D. F.; Chill, S. T.; Zhang, L.; Frenkel, A. I.; Henkelman, G.; Crooks, R. M. A Theoretical and Experimental Examination of Systematic Ligand-Induced Disorder in Au Dendrimer-Encapsulated Nanoparticles. *Chem. Sci.* **2013**, *4*, 2912–2921.

34. Matos, J.; Ono, L. K.; Behafarid, F.; Croy, J. R.; Mostafa, S.; DeLaRiva, A. T.; Datye, A. K.; Frenkel, A. I.; Roldan Cuenya, B. *In Situ* Coarsening Study of Inverse Micelle-Prepared Pt Nanoparticles Supported on γ-Al$_2$O$_3$: Pretreatment and Environmental Effects. *Phys. Chem. Chem. Phys.* **2012**, *14*, 11457–11467.

35. Rehr, J. J.; Kas, J. J.; Vila, F. D.; Prange, M. P.; Jorissen, K. Parameter-Free Calculations of X-ray Spectra with FEFF9. *Phys. Chem. Chem. Phys.* **2010**, *12*, 5503–5513.

36. Mistry, H.; Behafarid, F.; Bare, S. R.; Roldan Cuenya, B. Pressure-Dependent Effect of Hydrogen Adsorption on Structural and Electronic Properties of Pt/γ-Al$_2$O$_3$ Nanoparticles. *ChemCatChem* **2014**, *6*, 348–352.

37. van Bokhoven, J. A.; Louis, C.; Miller, J. T.; Tromp, M.; Safonova, O. V.; Glatzel, P. Activation of Oxygen on Gold/Alumina Catalysts: *In Situ* High-Energy-Resolution Fluorescence and Time-Resolved X-ray Spectroscopy. *Angew. Chem.* **2006**, *118*, 4767–4770.

38. van Bokhoven, J. A.; Miller, J. T. D Electron Density and Reactivity of the d-Band as a Function of Particle Size in Supported Gold Catalysts. *J. Phys. Chem. C* **2007**, *111*, 9245–9249.

39. Marcus, M.; Andrews, M.; Zegenhagen, J.; Bommannavar, A.; Montano, P. Structure and Vibrations of Chemically Produced Au$_{55}$ Clusters. *Phys. Rev. B* **1990**, *42*, 3312–3316.

40. Menard, L. D.; Xu, H.; Gao, S.-P.; Twesten, R. D.; Harper, A. S.; Song, Y.; Wang, G.; Douglas, A. D.; Yang, J. C.; Frenkel, A. I.; *et al.* Metal Core Bonding Motifs of Monodisperse Icosahedral Au$_{13}$ and Larger Au Monolayer-Protected Clusters as Revealed by X-ray Absorption Spectroscopy and Transmission Electron Microscopy. *J. Phys. Chem. B* **2006**, *110*, 14564–14573.

41. Zhang, P.; Sham, T. X-ray Studies of the Structure and Electronic Behavior of Alkanethiolate-Capped Gold Nanoparticles: The Interplay of Size and Surface Effects. *Phys. Rev. Lett.* **2003**, *90*, 245502.

42. Tsunoyama, H.; Tsukuda, T. Magic Numbers of Gold Clusters Stabilized by PVP. *J. Am. Chem. Soc.* **2009**, *131*, 18216–18217.

43. Ravel, B.; Newville, M. Athena, Artemis, Hephaestus: Data Analysis for X-ray Absorption Spectroscopy Using IFEFFIT. *J. Synchrotron Radiat.* **2005**, *12*, 537–541.

44. Newville, M. IFEFFIT: Interactive XAFS Analysis and FEFF Fitting. *J. Synchrotron Radiat.* **2001**, *8*, 322–324.

45. Ankudinov, A. L.; Rehr, J. J.; Conradson, S. D. Real-Space Multiple-Scattering Calculation and Interpretation of X-ray-Absorption Near-Edge Structure. *Phys. Rev. B* **1998**, *58*, 7565–7576.

46. Hohenberg, P. Inhomogeneous Electron Gas. *Phys. Rev.* **1964**, *136*, B864–B871.

47. Kohn, W.; Sham, L. J. Self-Consistent Equations Including Exchange and Correlation Effects. *Phys. Rev.* **1965**, *140*, A1133–A1138.

48. Blöchl, P. E. Projector Augmented-Wave Method. *Phys. Rev. B* **1994**, *50*, 17953–17979.

49. Kresse, G. Efficient Iterative Schemes for *Ab Initio* Total-Energy Calculations Using a Plane-Wave Basis Set. *Phys. Rev. B* **1996**, *54*, 11169–11186.

50. Kresse, G.; Hafner, J. *Ab Initio* Molecular Dynamics for Liquid Metals. *Phys. Rev. B* **1993**, *47*, 558–561.

51. Perdew, J. P.; Burke, K.; Ernzerhof, M. Generalized Gradient Approximation Made Simple. *Phys. Rev. Lett.* **1996**, *77*, 3865–3868.

52. Klimeš, J.; Bowler, D. R.; Michaelides, A. Van der Waals Density Functionals Applied to Solids. *Phys. Rev. B* **2011**, *83*, 195131.

53. Klimeš, J.; Bowler, D. R.; Michaelides, A. Chemical Accuracy for the van der Waals Density Functional. *J. Phys: Condens. Matter.* **2010**, *22*, 022201.

54. Cordero, B.; Gomez, V.; Platero-Prats, A. E.; Reves, M.; Echeverria, J.; Cremades, E.; Barragan, F.; Alvarez, S. Covalent Radii Revisited. *Dalton Trans.* **2008**, 2832–2838.